

Improvements to Target-Based 3D LiDAR to Camera Calibration

Jiunn-Kai Huang and Jessy W. Grizzle

Abstract—The homogeneous transformation between a LiDAR and monocular camera is required for sensor fusion tasks, such as SLAM. While determining such a transformation is not considered glamorous in any sense of the word, it is nonetheless crucial for many modern autonomous systems. Indeed, an error of a few degrees in rotation or a few percent in translation can lead to 20 cm translation errors at a distance of 5 m when overlaying a LiDAR image on a camera image. The biggest impediments to determining the transformation accurately are the relative sparsity of LiDAR point clouds and systematic errors in their distance measurements. This paper proposes (1) the use of targets of known dimension and geometry to ameliorate target pose estimation in face of the quantization and systematic errors inherent in a LiDAR image of a target, and (2) a fitting method for the LiDAR to monocular camera transformation that fundamentally assumes the camera image data is the most accurate information in one’s possession.

I. INTRODUCTION AND RELATED WORK

The desire to produce 3D-semantic maps with our Cassie-series bipedal robot presented in [1] and [2] has motivated us to fuse 3D-LiDAR and RGB-D monocular camera data for improved navigation. Indeed, by mapping spatial LiDAR points onto a segmented and labeled camera image, one can associate the label of a pixel (or a region about it) to the LiDAR point as shown in Fig. 1.

In this paper, we assume that the intrinsic calibration of the two sensors has already been done [3] and focus on obtaining the rigid transformation, i.e. rotation matrix and translation, between a LiDAR and camera. This is a well studied problem with a rich literature that can be roughly divided into methods that require targets: [4], [5], [6], [7], [8], [9], [10] and those that do not: [11], [12], [13], [14], [15]. Our modest contributions are applicable to methods that use planar polygonal targets, such as checkerboards, triangles, and diamonds.

In target-based methods, one seeks to estimate a set of target features (e.g., edge lines, normal vectors, vertices) in the LiDAR’s point cloud and the camera’s image plane. If “enough” independent correspondences can be made, the LiDAR to camera transformation can be found by Perspective-n-Point (PnP) as in [16], that is, though an optimization problem of the form

$$(R_C^{L*}, T_C^{L*}) = \arg \min_{(R, T)} \text{dist}(P(H_L^C(X_i)), Y_i), \quad (1)$$

where X_i are the (homogeneous) coordinates of the LiDAR features, Y_i are the coordinates of the camera features, P is the oft-called “projection map”, H_L^C is the (homogeneous

Jiunn-Kai Huang and J. Grizzle, are with the Robotics Institute, University of Michigan, Ann Arbor, MI 48109, USA. {bjhuang, grizzle}@umich.edu.



Fig. 1: Using the obtained transformation, LiDAR points are mapped onto a semantically segmented image. Each point is associated with the label of a pixel. The road is marked as white; static objects such buildings as orange; the grass as yellow-green, and dark green indicates trees.

representation of) the LiDAR-frame to camera-frame transformation with rotation matrix R_C^L and translation T_C^L , and dist is a distance or error measure.

A. Rough Overview of the Most Common Target-based Approaches

The works closest to ours are [17], [18]. Each of these works has noted that rotating a square target so that it presents itself as a diamond can help to remove pose ambiguity due to the spacing of the ring lines; in particular, see Fig. 2 in [17] and Fig. 1 in [18]. More generally, we recommend the literature overview in [17] for a recent, succinct survey of LiDAR to camera calibration.

The two most common sets of features in the area of target-based calibration are (a) the 3D-coordinates of the vertices of a rectangular or triangular planar target, and (b) the normal vector to the plane of the target and the lines connecting the vertices in the plane of the target. Mathematically, these two sets of data are equivalent: knowing one of them allows the determination of the other. In practice, focusing on (b) leads to use of the SVD to find the normal vector and more broadly to least squares line fitting problems [18], while (a) opens up other perspectives, as highlighted in [17].

Figure 2a shows a 3D view of 25 scans from a factory-calibrated 32-Beam Velodyne ULTRA Puck LiDAR on a diamond shaped planar target, with a zoom provided in Fig. 2b. There are clearly systematic errors in the distance (or depth) measurement of the target, and these errors affect the estimation of the target’s “centroid”, which is commonly used to determine the translation of the target from the LiDAR and the target’s “normal vector”, which is used to define the plane of the target as in Fig. 2c. Subsequently, the point cloud is orthogonally projected to this plane and the line boundaries of the target are found by performing *ransac* on the appropriate set of ring edges; see Fig. 2d. The lines along the target’s boundaries then define its vertices in the

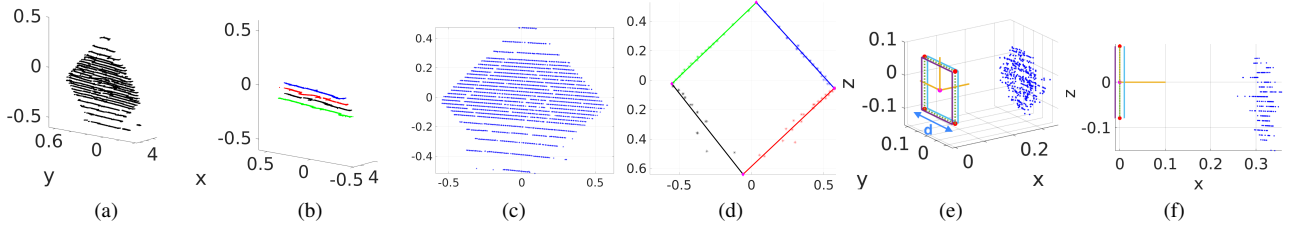


Fig. 2: (a) Twenty five LiDAR scans of a planar target. The point cloud is roughly 7 cm thick. (b) The “noise” in the point cloud is not random. A zoom for four of the rings (13, 15, 17, 19) is typical and shows systematic errors in distance. (c) LiDAR points orthogonally projected to the plane defined by the normal. (d) Example edge points selected to regress a line via *ransac*. (e) Target reference frame and real point cloud data. The dotted blue square is the reference target; its vertices are denoted $\{\bar{X}_i\}_{i=1}^4$. (f) A side-($x-z$)-view highlighting the non-zero thickness of a typical point cloud. These figures and all others in the paper are of sufficient resolution that they can be blown up to see detail.

plane, which for later reference, we note are not constrained to be compatible with the target’s geometry.

Once the vertices in the plane of the target have been determined, then knowledge of the target’s normal allows the vertices to be lifted back to the coordinates of the point cloud. This process may be repeated for multiple scans of a target, aggregates of multiple scans of a target, or several targets, leading to a list of target vertices $\{X_i\}_{i=1}^{4n}$, where n is the number of target poses.

The target is typically designed so that the vertices are easily distinguishable in the camera image. Denoting their corresponding coordinates in the image plane by $\{Y_i\}_{i=1}^{4n}$ completes the data required for the conceptual fitting problem in (1). While the problem is nonlinear and non-convex, this is typically not a problem because CAD data can provide an adequate initial guess for local solvers, such as Levenberg–Marquardt; see [18] for example.

B. Our Contributions

Our contributions can be summarized as follows.

- (a) We make use of the target’s geometry when estimating its vertices. In particular, if the target is a diamond, vertices form right angles and the lengths of the sides are equal. We show that this simple change improves the accuracy of estimating the vertices. Essentially, the extra constraints allow all of the target’s boundary points to be pulled into the regression problem at once, instead of parsing them into individual edges of the target, where small numbers of points on some of the edges will accentuate the quantization effects due to sparsity in a LiDAR point cloud.
- (b) We introduce a novel method for estimating the rigid body transform from target to LiDAR, H_T^L . For the point cloud pulled back to the LiDAR frame via the current estimate of the transformation, the cost is defined as the sum of the distance of a point to a 3D-reference target¹ in the LiDAR frame, for those points landing outside of the reference target, and zero otherwise. We use an L_1 -inspired norm in this work to define distance. As in [18], we find that this is less sensitive than using the L_2 -norm.

¹It has been given non-zero volume.

- (c) We exploit the fact that the variance of the camera data is significantly lower than that of the LiDAR data. Hence, after the LiDAR to camera transformation has been estimated by solving the PnP problem, we introduce a refinement step to the estimated pose of the LiDAR target given the current estimate of the LiDAR to camera transformation. In this process, the modified vertices remain consistent with the target geometry and the target’s point cloud.
- (d) We provide a round-robin validation study to support our approach. Once again, we place our faith in the camera image and use it as a proxy for ground truth. In the context of 3D semantic mapping, this makes sense.
- (e) Our code is released as [open source](#).

II. FINDING THE LiDAR TARGET VERTICES

In this conference version of the work, we will assume that each target is planar, square, and rotated in the frame of the LiDAR by roughly 45° to form a diamond as in Fig. 2a. As indicated in [17], [18], placing the targets so that the rings of the LiDAR run parallel to its edges leads to ambiguity in the vertical position due to the spacing of the rings. We assume that standard methods have been used to automatically isolate the target’s point cloud [19] and speak no further about it.

We take as a target’s features its four vertices, with their coordinates in the LiDAR frame denoted $\{X_i\}_{i=1}^4$; when useful, we abuse notation and pass from ordinary coordinates to homogeneous coordinates without noting the distinction. The vertices $\{X_i\}_{i=1}^4$ are of course not directly observable in the point cloud. This section will provide a new method for estimating their coordinates in the frame of the LiDAR using an L_1 -like norm. It will also provide a simple improvement to existing methods that use least squares fitting.

A. Remarks on LiDAR Point Clouds

LiDARs have dense regions and sparse regions along the z-axis, as shown in Fig. 2c. For a 32-beam Velodyne Ultra Puck, we estimate the resolution along the z-axis is 0.33° and 1.36° in the dense and sparse regions, respectively. A point’s distance resolution along the y-axis is roughly 0.1° . Figure 3a shows that a 1° of rotation error on each axis and 5% error in translation can significantly degrade a calibration

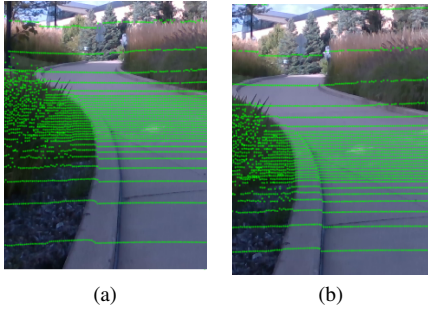


Fig. 3: (a) shows that a calibration result is not usable if it has few degrees of rotation error and a few percent of translation error. (b) shows good alignment of LiDAR point cloud on the image.

result. As noted in [17], [18], it is essential to place a target at an appropriate angle so that known geometry can mitigate quantization error in the y - and z -axes. To overcome quantization error in the x -axis, we accumulate a few scans to estimate a target's pose and “condition on” the current estimate of LiDAR to image plane projection matrix to refine the target's pose.

B. New Method for Determining Target Vertices

Let \mathcal{PC} denote the LiDAR point cloud and let the collection of 3D points be \mathcal{X}_i so that $\mathcal{PC} = \{\chi_i\}_{i=1}^N$. The objective is to fit a reference target with vertices $\{\bar{X}_i\}_{i=1}^4$, defined as in Fig. 2e, onto the point cloud with “minimum error”. It is actually easier to pull the \mathcal{PC} to the origin of the LiDAR through the current estimate of the inverse transformation $H_T^L := (H_L^T)^{-1}$ and measure the error there.

Remark 1. *To be clear, what we seek is a “best estimate” of the target vertices in the LiDAR frame and not the transformation itself. Our method is indirect because from the point cloud, we estimate a “best” LiDAR to target transformation, call it H_L^{T*} , and use it to define the vertices*

$$X_i^* := H_L^{T*}(\bar{X}_i), \quad 1 \leq i \leq 4. \quad (2)$$

The correspondences of the estimated vertices with the physical top, bottom, and left or right sides of the target are not needed at this point. ■

For $a \geq 0$ and $\lambda \in \mathbb{R}$, define

$$c(\lambda, a) := \begin{cases} \min\{|\lambda - a|, |\lambda + a|\} & \text{if } |\lambda| > a \\ 0 & \text{otherwise} \end{cases}; \quad (3)$$

see also the “soft L_1 norm” in [18]. Let $\{\tilde{\chi}_i\}_{i=1}^N := H_T^L(\mathcal{PC}) := \{H_T^L(\chi_i)\}_{i=1}^N$ denote the pullback of the point cloud by H_T^L , and denote a point's (x, y, z) -entries by $(\tilde{x}_i, \tilde{y}_i, \tilde{z}_i)$. The cost is defined as

$$C(H_T^L(\mathcal{PC})) := \sum_{i=1}^N c(\tilde{x}_i, \epsilon) + c(\tilde{y}_i, d/2) + c(\tilde{z}_i, d/2), \quad (4)$$

where $\epsilon \geq 0$ is a tuning parameter to account for uncertainty in the depth measurement of the planar target; see Fig. 2f.

We propose to determine the optimal H_T^L by

$$H_T^{L*} := \arg \min_{L \tilde{R}_T^L, L \tilde{T}_T^L} C(H_T^L(\mathcal{PC})). \quad (5)$$

Once the transformation is determined, the target vertices are defined by $X_i := (H_T^{L*})^{-1}(\bar{X}_i)$, $i = 1, \dots, 4$, as in Remark 1.

C. Improvement to Least Squares Approaches for Finding the Target Vertices

We assume the target's normal vector has been estimated using methods in [17], [18] and that the point cloud \mathcal{PC} has been orthogonally projected to the plane of the target. In [17], [18], lines along the four edges of the projected target are regressed individually after appropriately parsing the edge points. For “robustness”, *ransac* is typically used.

Instead, we propose to use all of the edge points simultaneously when regressing the edges. The basic formulation remains one of fitting four lines to the four sets of edge points, as is standard in the area,

$$z = m_i y + b_i, \quad 1 \leq i \leq 4 \quad (6)$$

and then adding in the constraints for a square. For opposite sides to be parallel, one needs

$$m_1 = m_3, \quad m_2 = m_4, \quad (7)$$

and to form right angles,

$$m_1 m_2 = -1. \quad (8)$$

The least squares line-fitting problem with (7) is a QP and already allows edges on opposite sides of the diamond to contribute to finding the slopes. While the constraint (8) links all the edges together, it makes the least squares problem non-convex. However, applying Taylor's theorem about “current estimates” of the slopes at step t , denoted m_1^t, m_2^t , along with some simple algebra results in the linear (update) constraint

$$\begin{bmatrix} m_2^t & m_1^t \end{bmatrix} \begin{bmatrix} m_1^{t+1} \\ m_2^{t+1} \end{bmatrix} = -1 + m_1^t m_2^t. \quad (9)$$

Starting with the initial estimates of $m_1^0 = 1, m_2^0 = -1$, in our experience, iterating the QP with linear constraints

$$A_{eq} = \begin{bmatrix} 1 & 0 & -1 & 0 \\ 0 & 1 & 0 & -1 \\ m_2^t & m_1^t & 0 & 0 \end{bmatrix}, \quad b_{eq} = \begin{bmatrix} 0 \\ 0 \\ -1 + m_1^t m_2^t \end{bmatrix} \quad (10)$$

on the slopes, and no constraints on the offsets, converges in two or three steps. In principle, one should also impose conditions on the offsets b_i so that the lengths of the sides are equal to the physical size of the target, but in our experience, it is not necessary to do this.

The intersections of the resulting lines define the target's vertices in the plane defined by its normal vector. It is then straightforward to lift them to vertices $\{X_i\}_{i=1}^4$ of the target in \mathbb{R}^3 . The reader is referred to [20] for the corresponding transformation, H_L^T .

III. VERTICES IN THE IMAGE PLANE AND CORRESPONDENCES WITH THE LiDAR VERTICES

For a given camera image of a LiDAR target, let $\{{}_C Y_i\}_{i=1}^4$ denote the vertices of the camera image. We assume

that these have been obtained through the user's preferred method, such as corner detection [21], [22], [23], edge detection [24], [25], [26], or even manual selection. This is not the hard part of the calibration problem. To achieve simple correspondences $X_i \leftrightarrow {}_C Y_i$, the order of the indices on $\{X_i\}_{i=1}^4$ may need to be permuted; we use the vertical and horizontal positions to sort them.

Once we have the correspondences, the next step is to project the vertices of the LiDAR target, $[x_i \ y_i \ z_i \ 1]^T = X_i$, into the image coordinates. The standard relations are [27], [28]

$$\begin{bmatrix} u' \\ v' \\ w' \end{bmatrix} = \begin{bmatrix} f_x & s & c_x \\ 0 & f_y & c_y \\ 0 & 0 & 1 \end{bmatrix} \begin{bmatrix} 1_{3 \times 3} \\ \mathbf{0}_{1 \times 3} \end{bmatrix}^T \begin{bmatrix} R_L^C & T_L^C \\ \mathbf{0}_{1 \times 3} & 1 \end{bmatrix} \begin{bmatrix} x_i \\ y_i \\ z_i \\ 1 \end{bmatrix} \quad (11)$$

$${}_L Y_i = [u \ v \ 1]^T = \left[\frac{u'}{w'} \ \frac{v'}{w'} \ 1 \right]^T, \quad (12)$$

where (11) includes the camera's intrinsic parameters and the extrinsic parameters (R_L^C, T_L^C) that we seek.

For later use, we combine (11) and (12) to define

$$\Pi(X_i; R_L^C, T_L^C) := {}_L Y_i, \quad (13)$$

the projection from LiDAR coordinates to image coordinates. Note that it is a function of both the extrinsic variables and the LiDAR point cloud.

IV. EXTRINSIC OPTIMIZATION AND POSE REFINEMENT

This section assumes the vertices of the target in the LiDAR frame and in the camera's image plane have been determined, along with their correspondences.

A. Extrinsic Transformation Optimization

The optimization for the extrinsic transformation can be formulated in two ways: minimize Euclidean distance of the corresponding corners or maximize the intersection over union (IoU) of the corresponding polygons.

1) *Euclidean distance*: The standard PnP formulation is

$$(R_L^{C*}, T_L^{C*}) := \arg \min_{R, T} \sum_{i=1}^{4n} \|\Pi(X_i; R, T) - {}_C Y_i\|_2^2 \quad (14)$$

$$= \arg \min_{R, T} \sum_{i=1}^{4n} \|{}_L Y_i - {}_C Y_i\|_2^2, \quad (15)$$

where ${}_C Y_i \in \mathbb{R}^2$ are the camera corners, ${}_L Y_i \in \mathbb{R}^2$ are defined in (13), and n is the number of target poses.

2) *IoU optimization*: To compute the IoU of two projected polygons of the targets in an image plane, we define the intersection as a polygon with known coordinates². We sort the vertices of the polygon counterclockwise using Graham scan, a method to find the convex hull of a finite set of points on a plane [29], [30]. The intersection area of the polygon can be calculated via the Shoelace algorithm [31].

²The vertices of the polygon consist of the 2D corners and the 2D line intersections and thus can be computed efficiently.

B. Refinement of the LiDAR Target Vertices

The above methods optimize (R_L^C, T_L^C) for given values of $\{X_i\}_{i=1}^{4n}$. Due to the systematic errors mentioned in Sec.II-A, we suspect the LiDAR vertices are less accurate than those of the camera's image. We therefore propose a refinement of the vertices conditioned on the current estimate of the projection map, Π , in (13), that is, based on the current estimate of the extrinsic parameters (R_L^C, T_L^C) . Once the vertices are updated, new estimates for (R_L^C, T_L^C) can be obtained, giving us an alternating two-step process:

Step 1: Adjust vertices with current ${}^t R_L^C, {}^t T_L^C$ held fixed

$$\begin{aligned} \delta H := & \begin{bmatrix} \delta R & \delta T \\ 0 & 1 \end{bmatrix} \\ \delta H^* := & \arg \min_{\delta H} \sum_{i=1}^{4n} \|\Pi(\delta H \circ {}^t X_i; {}^t R_L^C, {}^t T_L^C) - {}_C Y_i\|_2^2 \\ & + \rho C((H_L^T \circ \delta H)^{-1}(\mathcal{PC})); \text{ and} \end{aligned} \quad (16)$$

Step 2: Refine calibration R_L^C, T_L^C using updated vertices

$$\begin{aligned} {}^{t+1} X_i := & \delta H^* \circ {}^t X_i \\ {}^{t+1} Y_i = & \Pi({}^{t+1} X_i; {}^t R_L^C, {}^t T_L^C), \\ {}^{t+1} (R_L^{C*}, T_L^{C*}) = & \arg \min_{R, T} \sum_{i=1}^{4n} \|{}^{t+1} Y_i - {}_C Y_i\|_2^2, \end{aligned} \quad (17)$$

where superscript t denotes iteration number, X_i and ${}_C Y_i$ are as before, and the weight ρ trades off confidence in the point cloud vs the camera.

V. EXPERIMENTAL RESULTS

In this section, we extensively evaluate our proposed methods on seven different scenes though a form of "cross-validation": in a round-robin fashion, we train on one scene and then evaluate on the other six. The quantitative evaluation consists of computing pixel error per corner, where we take the image vertices as ground truth. We also show qualitative validation results by projecting the LiDAR scans onto camera images; we include here as many as space allows, with more scenes and larger images available at [20].

A. Data Collection

The scenes include both outdoor and indoor settings. Each scene includes two targets, one approximately 80.5 cm square and the other approximately 15.8 cm square, with the smaller target placed closer to the camera-LiDAR pair. We use an *Intel RealSense Depth Camera D435* and a *32-Beam Velodyne ULTRA Puck LiDAR*, mounted on an in-house designed torso for a Cassie-series bipedal robot [2]. From the CAD file, the camera is roughly 20 cm below the LiDAR and 10 cm in front of it. The angle of the camera is adjustable. Here, its "pitch", in the LiDAR frame, is approximately zero. For each scene, we collect approximately 10 s of synchronized data, resulting in approximately 100 pairs of scans and images.

B. Data Processing

For each scene, 15 consecutive pairs of LiDAR scans and camera images are extracted and divided into 5 data sets.

For each data set, we apply three methods to estimate the vertices of the two targets:

- **RN:** Uses SVD to extract the normal and *ransac* for individual line fitting, with the vertices obtained as the intersections of the lines.
- **GN:** Uses SVD to extract the normal and the QP associated with (10) to fit a square.
- **GL₁:** Uses (5) and (2) to find the vertices.
- For each of these, we include the refinement step of Sec. IV-B, and denote them by **RN-R**, **GN-R**, and **GL₁-R**. For **GL₁-R**, the cost term in (16) is given by (4), while for the two least squares approaches, we measure the Euclidean norm of the 3D-edge points of the point cloud to the lines defined by the refined target vertices.

In all of the above, the least-squares-based PnP method of (14) is being used to find the extrinsic calibration. We also checked using the IoU (see Sec. IV-A.2), but because the results are similar, we are not reporting them here. The interested reader can consult [20]. SVD, *ransac*, and QP were computed using standard MATLAB commands, while the optimizations in (5), (14), (16) and (17) were done with *fmincon*.

C. Quantitative Results

Once again, we are taking the camera data as a proxy for ground truth. In Table I, we compute the RMS error of the LiDAR vertices projected into the image plane for each of the above methods as shown in Fig. 4. To be crystal clear, we are reporting

$$\sqrt{\frac{1}{4n} \sum_{i=1}^{4n} \|_L Y_i - C Y_i \|_2^2}, \quad (18)$$

where $4n = 40$ is the total number of target corners. Hence, the units are pixel per corner.

VI. QUALITATIVE RESULTS AND DISCUSSION

In LiDAR to camera calibration, due to the lack of ground truth, it is traditional to show projections of LiDAR point clouds onto camera images. Often it is unclear if one is viewing training data or validation data. In Figure 5, we show a set of projections of LiDAR point clouds onto camera images for validation data. An additional set of images can be found in [20]. All of them show that the key geometric features in the image and point cloud are well aligned and will allow us to achieve our goal of 3D semantic mapping with our bipedal robot Cassie Blue.

Table I shows that **GL₁** and **GL₁-R** outperform the other methods. We conjecture that **GL₁** outperforms the least-squares methods because it avoids estimating a normal vector for the target's point cloud. The systematic variations in the target depth may be rendering the normal computation inaccurate. We conjecture that the refinement method did not provide significant improvement to **GL₁** because the errors were already so small.

Imposing geometry when fitting the edges improves the least-square methods. Moreover, refining the target vertices in the LiDAR point cloud on the basis of the camera data also proved useful. We emphasize these points because one



Fig. 4: Visual depiction of the validation data in the last row of Table I. For the method **GL₁-R**, five sets of estimated LiDAR vertices for each target have been projected into the image plane and marked in green, while the target's point cloud has been marked in red. Blowing up the image allows the numbers reported in the table to be visualized. The vertices are key.

may be able to use them to improve several current packages for extrinsic calibration. The main concerning point of the data is the variability in the least squares results.

Throughout the paper, we have avoided the term “automatic” in regards to our calibration method. Could it be applied? Perhaps the reviewers will have an opinion. We have released the MATLAB-version of our software with this submission. The only manual intervention required is, once the image edges have been detected using the `edge` command in MATLAB with the ‘Canny’ option, we manually click the target corners to obtain their coordinates. This will be automated soon.

VII. CONCLUSIONS

We proposed improvements to target-based LiDAR-camera calibration. We evaluated our proposed methods and compared them with other approaches in a round-robin validation study. In the validation study, our L_1 -based method achieved a per corner RMS error, measured in the image plane, on the order of a few pixels, when comparing the projected LiDAR vertices to the image corners. The validation results show our methods are repeatable and outperform other target-based methods.

ACKNOWLEDGMENT

Funding for this work was provided by the Toyota Research Institute (TRI) under award number N021515. Funding for J. Grizzle was in part provided by TRI and in part by NSF Award No. 1808051. This article solely reflects the opinions and conclusions of its authors and not the funding entities. Dr. M Ghaffari offered advice during the course of this project. The first author thanks Wonhui Kim for useful conversations and Ray Zhang for generating the semantic image.

TABLE I: Round-robin validation study. The gray box denotes the training set and the others are used as validation data. The numbers are the RMS errors of the LiDAR vertices projected to the image plane in pixels per corner; see (18).

Training\Validation	Method	S1	S2	S3	S4	S5	S6	S7
S1	RN	181.316	93.736	111.898	158.531	57.896	96.584	167.754
	RN-R	182.252	84.828	102.918	138.973	43.536	83.368	155.562
	GN	181.315	66.953	79.913	50.607	113.239	57.896	96.584
	GN-R	182.252	60.586	73.497	47.483	99.270	48.017	85.850
	GL ₁	1.546	1.465	1.437	1.685	0.880	1.098	1.986
	GL ₁ -R	1.443	1.383	1.398	1.590	0.775	0.918	1.772
S2	RN	147.794	108.470	115.953	110.759	75.704	93.869	122.773
	RN-R	142.731	111.257	118.454	110.603	77.741	92.488	122.332
	GN	18.007	16.077	14.940	14.299	7.581	13.920	21.746
	GN-R	16.210	12.468	15.037	14.099	7.181	9.343	19.752
	GL ₁	1.196	1.470	1.712	1.667	0.944	2.040	3.255
	GL ₁ -R	1.021	1.322	1.589	1.465	0.823	1.772	2.781
S3	RN	82.742	77.428	126.157	118.209	68.545	98.988	126.225
	RN-R	83.433	68.193	99.310	90.852	58.459	76.674	106.206
	GN	12.165	12.599	10.902	11.138	6.491	11.071	11.649
	GN-R	11.948	12.325	8.951	10.924	5.657	10.826	10.661
	GL ₁	2.552	2.911	8.288	3.513	2.349	4.595	8.136
	GL ₁ -R	1.880	2.308	6.115	2.580	1.750	3.346	6.996
S4	RN	97.964	159.075	102.341	102.541	151.029	149.366	143.103
	RN-R	69.939	118.571	72.065	101.823	108.226	104.654	122.885
	GN	38.250	49.452	36.823	6.536	35.846	32.127	52.071
	GN-R	37.189	48.737	35.937	5.224	35.268	31.653	51.421
	GL ₁	1.576	1.538	1.678	0.608	1.390	1.321	1.071
	GL ₁ -R	1.494	1.472	1.623	0.564	1.319	1.303	1.075
S5	RN	123.945	97.514	132.301	114.755	177.790	90.855	124.152
	RN-R	112.834	86.316	119.455	100.701	177.249	83.311	110.449
	GN	14.275	17.187	14.252	8.145	5.288	10.748	19.338
	GN-R	14.222	17.025	14.219	8.046	4.425	10.530	18.951
	GL ₁	1.444	1.159	1.390	1.706	1.444	1.696	3.306
	GL ₁ -R	1.421	1.193	1.396	1.754	1.038	1.748	3.394
S6	RN	73.994	103.545	92.773	111.625	98.759	48.956	106.110
	RN-R	49.349	67.209	54.542	58.689	59.899	47.769	68.004
	GN	18.824	19.057	18.689	11.423	15.200	6.353	16.714
	GN-R	11.873	11.725	12.174	7.362	9.299	2.752	9.462
	GL ₁	2.895	2.486	3.064	1.102	2.102	1.226	2.348
	GL ₁ -R	2.717	2.351	2.912	1.087	2.004	1.142	2.272
S7	RN	39.186	52.019	39.212	33.833	42.461	32.617	66.453
	RN-R	60.400	81.536	62.063	64.880	74.975	65.332	66.973
	GN	57.494	72.737	57.880	51.469	65.373	54.498	86.117
	GN-R	57.494	78.133	61.472	57.484	71.180	54.498	86.117
	GL ₁	0.707	0.963	1.163	1.180	0.923	0.949	1.682
	GL ₁ -R	0.692	0.936	1.139	1.144	0.899	0.933	1.616



Fig. 5: Qualitative validation results. For the method **GL₁-R** trained on S₁, the LiDAR point cloud has been projected into the image plane for the other alignment can be best judged. The reader may find other areas of interest. Enlarge in your browser for best viewing.

REFERENCES

- [1] Y. Gong, R. Hartley, X. Da, A. Hereid, O. Harib, J.-K. Huang, and J. Grizzle, “Feedback control of a cassie bipedal robot: Walking, standing, and riding a segway,” in *2019 American Control Conference (ACC)*. IEEE, 2019, pp. 4559–4566.
- [2] J. Huang. (2019) Cassie Blue walks Around the Wavefield. <https://youtu.be/LhFC45jweFMc>.
- [3] F. M. Mirzaei, D. G. Kottas, and S. I. Roumeliotis, “3D LiDAR-camera intrinsic and extrinsic calibration: Identifiability and analytical least-squares-based initialization,” *The International Journal of Robotics Research*, vol. 31, no. 4, pp. 452–467, 2012.
- [4] X. Gong, Y. Lin, and J. Liu, “3D LiDAR-camera extrinsic calibration using an arbitrary trihedron,” *Sensors*, vol. 13, no. 2, pp. 1902–1918, 2013.
- [5] A. Dhall, K. Chelani, V. Radhakrishnan, and K. M. Krishna, “LiDAR-camera calibration using 3D-3D point correspondences,” *arXiv preprint arXiv:1705.09785*, 2017.
- [6] S. Verma, J. S. Berrio, S. Worrall, and E. Nebot, “Automatic extrinsic calibration between a camera and a 3D LiDAR using 3D point and plane correspondences,” *arXiv preprint arXiv:1904.12433*, 2019.
- [7] J. Jiao, Q. Liao, Y. Zhu, T. Liu, Y. Yu, R. Fan, L. Wang, and M. Liu, “A novel dual-LiDAR calibration algorithm using planar surfaces,” *arXiv preprint arXiv:1904.12116*, 2019.
- [8] E.-S. Kim and S.-Y. Park, “Extrinsic calibration of a camera-LiDAR multi sensor system using a planar chessboard,” in *2019 Eleventh International Conference on Ubiquitous and Future Networks (ICUFN)*. IEEE, 2019, pp. 89–91.
- [9] C. Guindel, J. Beltrán, D. Martín, and F. García, “Automatic extrinsic calibration for LiDAR-stereo vehicle sensor setups,” in *2017 IEEE 20th International Conference on Intelligent Transportation Systems (ITSC)*. IEEE, 2017, pp. 1–6.
- [10] A.-I. García-Moreno, J.-J. Gonzalez-Barbosa, F.-J. Ornelas-Rodriguez, J. B. Hurtado-Ramos, and M.-N. Primo-Fuentes, “LiDAR and panoramic camera extrinsic calibration approach using a pattern plane,” in *Mexican Conference on Pattern Recognition*. Springer, 2013, pp. 104–113.
- [11] G. Pandey, J. R. McBride, S. Savarese, and R. M. Eustice, “Automatic targetless extrinsic calibration of a 3D LiDAR and camera by maximizing mutual information,” in *Twenty-Sixth AAAI Conference on Artificial Intelligence*, 2012.
- [12] Z. Taylor and J. Nieto, “Automatic calibration of LiDAR and camera images using normalized mutual information,” in *Robotics and Automation (ICRA), 2013 IEEE International Conference on*, 2013.
- [13] J. Jeong, Y. Cho, and A. Kim, “The road is enough! extrinsic calibration of non-overlapping stereo camera and LiDAR using road information,” *IEEE Robotics and Automation Letters*, vol. 4, no. 3, pp. 2831–2838, 2019.
- [14] J. Jiang, P. Xue, S. Chen, Z. Liu, X. Zhang, and N. Zheng, “Line feature based extrinsic calibration of LiDAR and camera,” in *2018 IEEE International Conference on Vehicular Electronics and Safety (ICVES)*. IEEE, 2018, pp. 1–6.
- [15] W. Zhen, Y. Hu, J. Liu, and S. Scherer, “A joint optimization approach of LiDAR-camera fusion for accurate dense 3D reconstructions,” *IEEE Robotics and Automation Letters*, vol. 4, no. 4, pp. 3585–3592, 2019.
- [16] V. Lepetit, F. Moreno-Noguer, and P. Fua, “Epnp: An accurate $O(n)$ solution to the pnp problem,” *International journal of computer vision*, vol. 81, no. 2, p. 155, 2009.
- [17] Q. Liao, Z. Chen, Y. Liu, Z. Wang, and M. Liu, “Extrinsic calibration of LiDAR and camera with polygon,” in *2018 IEEE International Conference on Robotics and Biomimetics (ROBIO)*. IEEE, 2018, pp. 200–205.
- [18] L. Zhou, Z. Li, and M. Kaess, “Automatic extrinsic calibration of a camera and a 3D LiDAR using line and plane correspondences,” in *2018 IEEE/RSJ International Conference on Intelligent Robots and Systems (IROS)*. IEEE, 2018, pp. 5562–5569.
- [19] J.-K. Huang, M. Ghaffari, R. Hartley, L. Gan, R. M. Eustice, and J. W. Grizzle, “LiDARTag: A real-time fiducial tag using point clouds,” *arXiv preprint arXiv:1908.10349*, 2019.
- [20] J.K. Huang and Jessy W. Grizzle, “Extrinsic LiDAR Camera Calibration,” 2019. [Online]. Available: https://github.com/UMich-BipedLab/extrinsic_lidar_camera_calibration
- [21] C. G. Harris, M. Stephens, et al., “A combined corner and edge detector,” in *Alvey vision conference*, vol. 15, no. 50. Citeseer, 1988, pp. 10–5244.
- [22] E. Rosten and T. Drummond, “Machine learning for high-speed corner detection,” in *European conference on computer vision*. Springer, 2006, pp. 430–443.
- [23] E. Rosten, R. Porter, and T. Drummond, “Faster and better: A machine learning approach to corner detection,” *IEEE transactions on pattern analysis and machine intelligence*, vol. 32, no. 1, pp. 105–119, 2008.
- [24] J. Canny, “A computational approach to edge detection,” in *Readings in computer vision*. Elsevier, 1987, pp. 184–203.
- [25] J. S. Lim, “Two-dimensional signal and image processing,” *Englewood Cliffs, NJ, Prentice Hall*, 1990, 710 p., 1990.
- [26] O. R. Vincent, O. Folorunso, et al., “A descriptive algorithm for sobel image edge detection,” in *Proceedings of Informing Science & IT Education Conference (InSITE)*, vol. 40. Informing Science Institute California, 2009, pp. 97–107.
- [27] R. Hartley and A. Zisserman, “Multiple view geometry in computer vision second edition,” *Cambridge University Press*, 2000.
- [28] D. A. Forsyth and J. Ponce, *Computer vision: a modern approach*. Prentice Hall Professional Technical Reference, 2002.
- [29] R. L. Graham, “An efficient algorithm for determining the convex hull of a finite planar set,” *Info. Pro. Lett.*, vol. 1, pp. 132–133, 1972.
- [30] A. M. Andrew, “Another efficient algorithm for convex hulls in two dimensions,” *Information Processing Letters*, vol. 9, no. 5, pp. 216–219, 1979.
- [31] B. Braden, “The surveyor’s area formula,” *The College Mathematics Journal*, vol. 17, no. 4, pp. 326–337, 1986.